JOURNAL OF EXPERIMENTAL HEAT TRANSFER

# Heat Transfer Measurements in a Hydrogen-Oxyfuel Combustor

Tom Tanneberger[a] and Panagiotis Stathopoulos[b]

[a]Chair of Fluid Dynamics, Technische Universität Berlin, Müller-Breslau-Str.8, 10623 Berlin;

[b]Chair of Unsteady Thermodynamics in Gas Turbine Processes, Technische Universität Berlin, Müller-Breslau-Str.8, 10623 Berlin

**ARTICLE HISTORY**

Compiled July 13, 2020

Corresponding Author: Panagiotis Stathopoulos. Email: Panagiotis.Stathopoulos@TU-Berlin.de

**ABSTRACT**

In the context of emission-free electricity generation, the authors developed a novel hydrogen-oxygen combustor, which is based on swirl-stabilized combustion technology and steam dilution. Following previous burner characterization, the current study investigates the heat transfer conditions in the combustion chamber wall. To this end, a carefully controlled co-flow of air is used to cool the combustion chamber in an annular duct, which surrounds it. Temperature measurements enable the evaluation of the heat flux from the combustor flow to the walls, local wall temperatures, and the Nusselt numbers on the hot and the cold side. The extremely high wall temperatures, caused by the $H_2/O_2$ flame, can be reduced by steam dilution down to approximately 900 K. Even better cooling could be reached by using the dilution steam as the coolant before it flows to the plenum. The Nusselt numbers at the inner combustion chamber wall are in the order of $10 - 50$ and increase with the thermal power and the steam dilution ratio.

**KEYWORDS**

Heat transfer; Oxy-fuel combustion; Hydrogen; Steam dilution

## 1. Introduction

It is common understanding that greenhouse gas emissions must be reduced significantly to stop a severe climate crisis [1] and that this can only happen with a considerable expansion of renewable energy generation. The vast majority of renewables is not dispatchable and can potentially endanger grid reliability, when their share is increased. Besides primary and secondary control reserves, long term storage will be needed to shift any generation than cannot be consumed or transmitted at the time point of generation [2,3]. Power-to-gas is a promising solution for long-term energy storage. Here, excess energy from wind and solar, is used to generate pressurized $H_2$ from water with an electrolyser. The $H_2$ can be stored, transported, and converted back to energy when needed. **One opportunity to retrieve the energy is the direct combustion of the $H_2$.** Several projects on the combustion of hydrogen-rich fuels were initiated in the last years in industry [4–9]. However, these technologies still produce $NO_x$ and $CO_2$ emissions. The project, part of which the current work is, aims to develop and investigate a zero-emission $H_2$ combustion technology that burns $H_2$ and $O_2$ under stoichiometric conditions. Such a combustor can be installed in steam

power plants as an on-demand reheat stage [10], or it could be a part of a zero-emission power plant [11,12].

A few attempts have been made to investigate the internal combustion of $H_2$ and $O_2$ experimentally. A German consortium repurposed a rocket combustor into a 70 MW $H_2/O_2$ steam generator to be used as a steam cycle booster [13–17]. In this particular case, the combustor walls had to withstand a heat load of 15 to 20 $MW/m^2$. They were convectively cooled with water, which was injected and evaporated downstream of the combustion chamber to control the combustor outlet temperature. Insufficient combustion efficiency and wall cooling effects [17] led to the termination of this project. Similar projects have also been carried out in Russia [18–20] and Japan [21–23] with similar technical challenges.

In contrast to these projects, the current study applies the concept of steam-diluted (or wet) combustion to control the combustion temperature. Thus, the thermal stress of the combustion chamber can be reduced significantly compared to rocket combustors. This reduction results in less structural complexity and less fatigue, which is crucial for power plant utilization. The lab-scale burner in the current work builds upon an experimentally well-characterized design of a swirl-stabilized $H_2$/air burner [24–27], which was equipped with additional $O_2$ injectors. Preliminary results were reported by Schimek *et al.* [28] and Tanneberger *et al.* [29–31], who characterized the flow and flame behavior along with the combustion efficiency. **In the current paper, these investigations are extended by an analysis of the heat transfer in the combustion chamber.**

**In general, there are three ways of heat transfer, namely thermal conduction, thermal convection, and radiation. The major part of the heat released in the combustion chamber is convected in the axial direction by the exhaust flow. However, the heat transfer in the radial direction to the chamber walls is of high interest to estimate the heat loss and the material load. Hence, the analysis in this thesis focuses on the total heat transfer from the combustion gases to the combustion chamber wall caused by both conduction and radiation.**

**Different techniques to measure the heat transfer to the wall were re-**

**ported in the literature. Using an IR camera, Patil et al. [32] studied the heat transfer of a cold combustor flow by heating the wall and recording its temperature. The results showed that the Nusselt number was very high at the end of the secondary recirculation zones and then declined quickly downstream. A similar result was found by Hedlund und Ligrani [33] for the flow in a swirl chamber.**

**A second method was used by Back et al. [34,35] to study the heat transfer of hot combustion exhaust to a water-cooled nozzle wall.** They calculated the heat transfer coefficients from the coolant mass flow rate, the temperature increase, and the surface area. This steady-state calorimetric method was described in detail by Witte and Harper [36] and in the review of Bartz [37]. The same technique was utilized by Bělohradský et al. [38] to measure the heat transfer in a natural gas furnace combustion chamber. They reported a local maximum of the heat flux in the middle of the combustion chamber.

**The use of heat flux sensors is another option to determine heat transfer. For instance, Zhen et al. [39] measured the heat flux on a flame impingement plate at different nozzle-to-plate distances. Wu et al. [40] utilized water-cooled heat flux meters at the combustion chamber wall. Coaxial thermocouple heat flux gauges were employed by Jones et al. [41]. For the measurements in the current thesis, an approach similar to the calorimetric technique [35,37,38] is used, but with air as the cooling medium.**

**Instead of natural gas and air, the combustor in the current work runs on $H_2$ and $O_2$, which has a significant influence on the heat transfer. Bělohradský et al. [38] studied the impact of $O_2$ enrichment.** They found a significant increase of the heat flux – up to 46 % – when oxygen enrichment was applied and contributed this to enhanced radiation due to the higher $H_2O$ and $CO_2$ concentrations. Bäckström et al. [42] and Andersson et al. [43] came to the same conclusions by measuring the radiation heat transfer of oxygen-enriched flames optically. Baukal and Gebhart [44] additionally found that the radiant heat flux reaches its maximum value for stoichiometric flames with pure oxygen.

Zhen et al. [39] studied the effect of hydrogen enrichment up to 50 $\%_v$ to a premixed

LPG flame. While hydrogen had a massive impact on the emissions and shifted the point of maximum local heat flux closer to the nozzle, it had only a minor effect on the total heat transfer rate, which was increased by 3 %.

The effect of simultaneous $O_2$ and $H_2$ enrichment to a laminar methane diffusion flame was studied by Wu et al. [40]. They found that the radiative heat flux increased with the oxygen level, but decreased with increasing $H_2$ addition due to lower $CO_2$ and soot concentrations. The total heat flux, on the other hand, increased for both enrichments.

These effects also apply to the current study, in which the oxidizer is pure $O_2$ and the flue gas almost pure $H_2O$. Cremers et al. [45] analytically and numerically discussed the heat transfer of such $H_2/O_2$ flames. Measurements of the heat transfer in rocket combustors were reported by Droppers et al. [46] and Jones et al. [41]. Both studies aimed to provide databases for CFD validation.

**In the current work, for the first time the heat transfer to the wall is studied in an internal, steam-diluted $H_2/O_2$ combustor. The analysis has two distinct goals: the measurement of the total heat transfer to evaluate the effectiveness of the combustion chamber cooling, and the determination of spatially resolved wall temperatures and Nusselt numbers inside the combustion chamber, which are relevant for the further combustor development and power scaling.**

## 2. Experimental setup

### *2.1. Burner*

The combustor design builds upon that of swirl-stabilized gas turbine combustors. The main flow component is steam, which acts as a diluent for the chemical reaction and defines the flow field in the chamber. An azimuthal component is imposed on the steam flow to achieve aerodynamic flame stabilization. The burner has two independently controllable swirl generators (inner and outer swirler in Fig. 1). The swirl generators consist of tangential slots between the plenum and two coaxial annular ducts that channel the steam into the combustion chamber. The swirl intensity can be adjusted

separately by varying the blockage of the tangential slots (higher swirl for higher blockage ratio). The swirler blocking values for the configurations investigated in this work are given in Table 1.

Hydrogen is injected as a non-swirling jet on the central axis, surrounded by the inner steam stream coming from the inner swirl generator. Oxygen is injected through 30 coaxial holes between the inner and outer steam ducts. By this arrangement, $H_2$ and $O_2$ cannot form a combustible mixture near the combustor walls. Instead, they mix inside the combustion chamber, avoiding flashbacks. The swirled steam flow in the outer duct generates a jet that protects the reactants from the cold combustor wall to minimize its influence on the combustion efficiency.

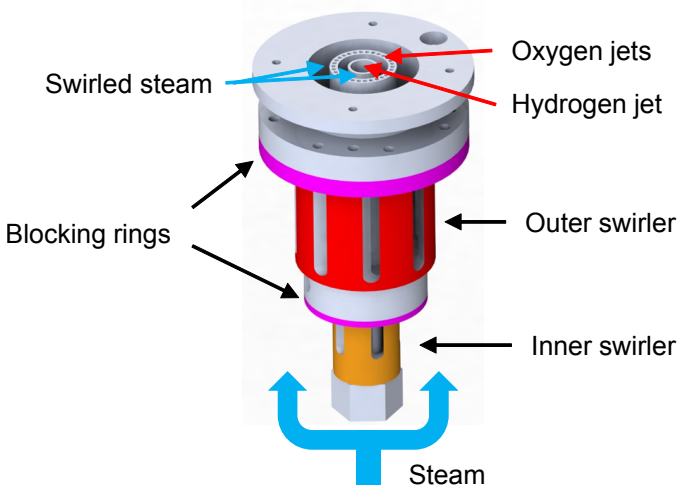


**Figure 1.** Drawing of the investigated generic burner.

**Table 1.** Burner configurations.

| Configuration | Inner swirler blocking % | Outer swirler blocking % |
|---|---|---|
| I | 11 | 25 |
| II | 61 | 25 |
| III | 61 | 50 |
| IV | 61 | 75 |

Tanneberger et al. [30] already studied the flow field, mixing properties and flame shapes of this combustor. In order to give the reader a better understanding of the physics in the combustion chamber, Figure 2 presents its flow field for two levels of steam dilution Ω. Ω is defined as the ratio of the reactant mass flows to the steam

mass flow used as a diluent (Eq. (1)).

$$\Omega = \frac{\dot{m}_{H_2} + \dot{m}_{O_2}}{\dot{m}_{steam}} \tag{1}$$

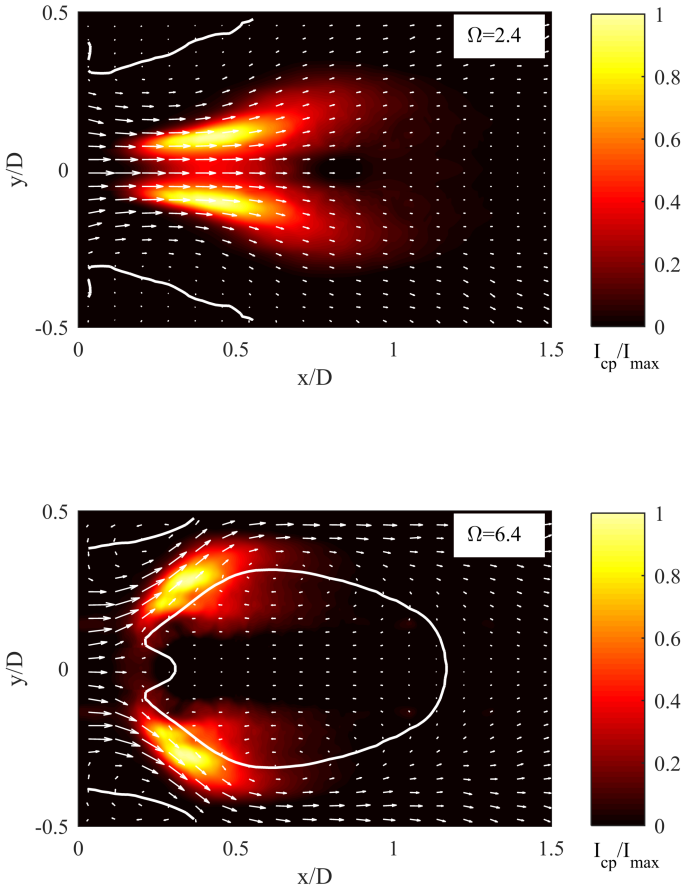


**Figure 2.** Relative OH* intensity of Configuration III in the center plane of the combustion chamber, superposed by quivers and the stagnation line of the velocity field, measured in a water tunnel [30].

The flow in the figure comes from the left and forms, in the case of high steam dilution, a swirl-induced central recirculation zone, indicated by the white bold contour line of zero axial velocity. The color in the plots visualizes the OH* intensity of the flame. It shows that a diffusion-stabilized jet flame establishes near the combustion chamber axis at low steam dilution. At high steam dilution, on the other hand, the flame stabilizes in the shear-layers of the recirculation zone. The study will refer to this type as the swirl-stabilized flame. For more detailed insights, please see the studies

mentioned above [26,30,31].

### *2.2. Combustion test rig*

The combustion tests are conducted at atmospheric pressure. A steam generator delivers super-heated steam to a plenum upstream of the burner at temperatures between 375 and 600 K. The combustion chamber is installed downstream of the burner, followed by a water-cooled exhaust tube. The combustion chamber has a diameter of 80 mm and a length of 220 mm of which 200 mm are actively cooled. Figure 3 shows the combustion chamber. It consists of a stainless steel (Type 1.4571) tube, which is surrounded by a second tube of sheet metal. The cooling air flows through this annular duct from four radial inlets. A valve controls the air mass flow rate with the help of a PID controller. A thermocouple **with an uncertainty of** $2.5°\mathbf{C}$ monitors the inlet temperature. The air enters the annular duct approximately 15 mm downstream of the combustor head. Two slotted sheet metals at the beginning and the end of the annulus distribute the air equally and enhance the turbulence intensity in the duct. Eight measurement points with Pt-100 temperature sensors **with an uncertainty of** $0.15°\mathbf{C}+0.2\,\%$ are distributed along the length of the annulus at a distance of 20 mm from each other. The sensor heads are placed **in the center of the annulus, about** 8 **mm away from the outer combustion chamber wall to ensure being outside of the thermal boundary layer. At three axial position, additional sensors are installed around the circumference.** The cooling chamber has two diagonally arranged outlets, which release the cooling air into the room. They feature a thermocouple $(\sigma = 2.5°\mathbf{C})$ each to record the outlet conditions. The outer surface of the annulus is thermally insulated to reduce heat losses to the environment. Table 2 gives the dimensions of the combustion chamber and the cooling system.

The combustor's exhaust temperature is measured by an unshielded thermocouple **with an uncertainty of** $0.75\,\%$ inside the exhaust tube, 280 mm downstream of the combustion chamber inlet.

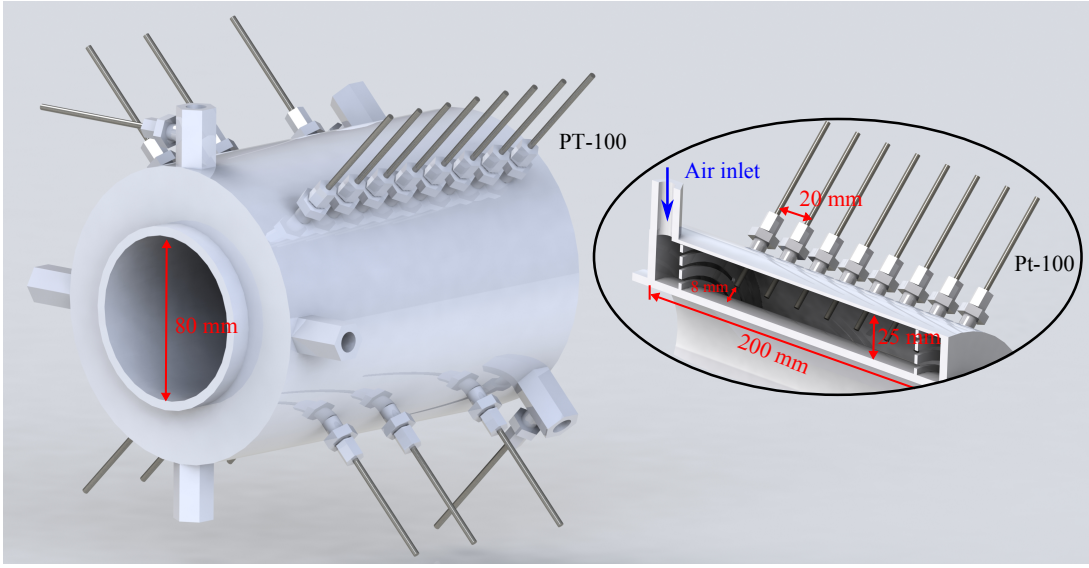


**Figure 3.** Air-cooled combustion chamber with PT-100 temperature sensors and dimensions. The left end of the metal tube is mounted directly to the burner head.

**Table 2.** Dimensions of combustion chamber.

| Combustor characteristics | | | |
|---|---|---|---|
| Length combustion chamber | $L_{cc}$ | 220 | mm |
| Length cooling section | $L_{duct}$ | 200 | mm |
| Diameter combustion chamber | $D$ | 80 | mm |
| Wall thickness | $s_w$ | 4.5 | mm |
| Inner diamter cooling duct | $d_{duct,i}$ | 89 | mm |
| Outer diameter cooling duct | $d_{duct,o}$ | 140 | mm |
| Hydraulic diameter cooling duct | $d_{duct,h}$ | 51 | mm |
| Cooling mass flow | $\dot{m}_{air}$ | 25 | kg/h |

## 3. Heat transfer analysis

The heat transfer analysis deploys two methods: a global heat balance and the cell method to determine the Nusselt number of the inner combustor flow along the length of the combustor. The thermal conductivity ($\lambda_w$) of the combustion chamber wall and the specific heat capacity and enthalpy of air and steam are taken from the VDI-Wärmeatlas [47] as a function of temperature.

### *3.1. Total heat balance*

The total heat balance compares the incoming and outgoing enthalpy fluxes. The combustion chamber and the cooling duct are treated as black boxes, as shown in Fig. 4.

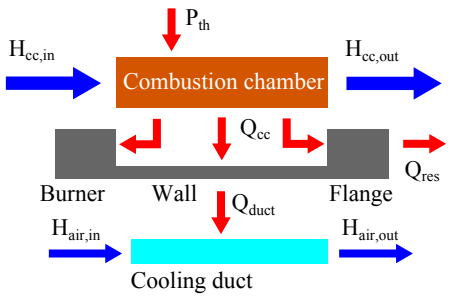


**Figure 4.** Schematic of the total heat transfer model.

At the inlet of the combustion chamber, three fluids enter, each with its specific enthalpy $h_{H_2O}(T_{plenum})$, $h_{H_2}$, and $h_{O_2}$. **The three inflows can be combined to the inlet enthalpy flux $\dot{H}_{cc,in}$, shown in Fig. 4. The steam enthalpy is evaluated at the burner plenum temperature, and the reactant enthalpies at room temperature.**

For the calculation of the outlet stream, perfect combustion is assumed. Hence, the exhaust gas is treated as pure steam, and the enthalpy of the exhaust flow $\dot{m}_{ex} = \dot{m}_{H_2O} + \dot{m}_{H_2} + \dot{m}_{O_2}$ is determined at the exhaust temperature $T_{ex}$.

The enthalpy fluxes in the combustion chamber read as follows.

$$\dot{H}_{cc,in} = \dot{m}_{H_2O} h_{H_2O}(T_{plenum}) + \dot{m}_{H_2} h_{H_2} + \dot{m}_{O_2} h_{O_2} \tag{2}$$

$$\dot{H}_{cc,out} = \dot{m}_{ex} h_{H_2O}(T_{ex}) \tag{3}$$

$$\Delta\dot{H}_{cc} = \dot{H}_{cc,out} - \dot{H}_{cc,in} \tag{4}$$

**The enthalpy in the combustion chamber increases due to the heat input of the flame. On the other hand, it decreases due to the heat loss of the system by heat conduction in the metal parts.** The heat loss is generally unknown and therefore, calculated from the total heat balance, i.e., the known $\Delta\dot{H}_{cc}$ and the thermal

power of the flame:

$$\dot{Q}_{cc} = \Delta\dot{H}_{cc} - P_{th}. \tag{5}$$

The combustion chamber is actively cooled by an air co-flow. The enthalpy gain of this flow is measured by its inlet and outlet temperature as:

$$\Delta\dot{H}_{duct} = \dot{m}_{air}\left(h_{air,out} - h_{air,in}\right). \tag{6}$$

The cooling duct is thermally insulated against its surroundings. Thus, heat losses by conduction are assumed to be low, and only the heat input from the combustion chamber wall is considered:

$$\dot{Q}_{duct} = \Delta\dot{H}_{duct}. \tag{7}$$

The conductive heat losses of the plenum, the duct, and the flanges should be low due to the thermal insulation. Nevertheless, they are not negligible because they disturb the heat balance of the system, i.e., $\dot{Q}_{cc} \neq -\dot{Q}_{duct}$. Hence, the estimated residual heat flux is

$$\dot{Q}_{res} = \dot{Q}_{cc} + \dot{Q}_{duct}. \tag{8}$$

**The exhaust temperature used in Eq.** (3) **is measured by an unshielded thermocouple. For very high exhaust temperatures, it starts to glow. Hence, the measured temperatures are corrected for the radiation heat loss of the thermocouple using a model proposed by Príkopský [48]. The correction is shown in Fig. 5 for an example flame at different steam dilution ratios.**

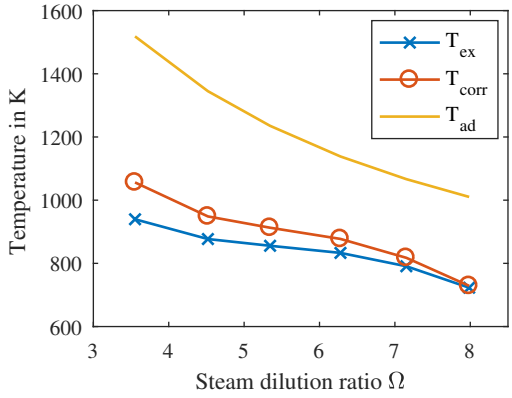


**Figure 5.** Correction of the Thermocouple measurements in the exhaust.

### *3.2. Heat Transfer through the Wall*

A network model using the cell method calculates the heat transfer through the wall. To this end, the cooling duct, the wall, and the combustion chamber are divided into seven cells of $L_{cell} = 20\,\mathrm{mm}$, as sketched in Fig. 6.

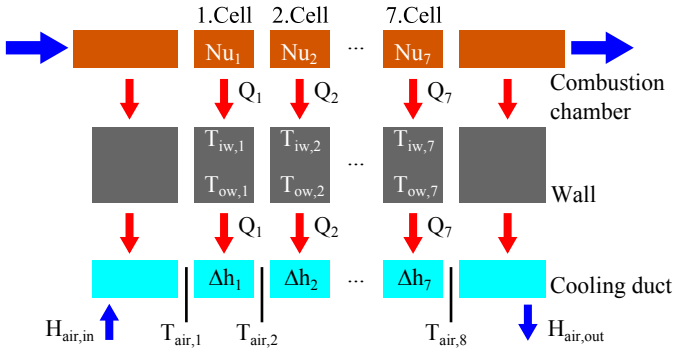


**Figure 6.** Schematic of the heat transfer network model.

**The temperature in the cooling duct is measured at the boundaries of each cell, as shown by the black lines in Fig. 6. Hence, the temperature difference of each cell can be calculated. It further yields the change of enthalpy $\Delta h_j$ in the cells and, thus, the heat flux $\dot{Q}_j$ to the cooling duct in each cell.**

$$\Delta h_j = cp_{air,j+1} T_{air,j+1} - cp_{air,j} T_{air,j} \tag{9}$$

$$\dot{Q}_j = \Delta h_j \dot{m}_{air} \tag{10}$$

**The heat flux into the cooling duct $\dot{Q}_j$ equals the amount of heat per cell conducted from the combustion chamber through the wall. The next step is to determine the wall temperature of the cells via the heat transfer coefficient $\alpha_j$. Therefore,** the modeling of the air wall interaction follows Chapter Gb of the VDI-Wärmeatlas [47].

$$\alpha_{air,j} = \frac{1}{\pi d_{duct,i} L_{cell}} \frac{\dot{Q}_j}{\Delta_{ln} T_{air,j}} \tag{11}$$

$$\Delta_{ln} T_{air,j} = \frac{(T_{ow,j} - T_{air,j}) - (T_{ow,j} - T_{air,j+1})}{\ln(T_{ow,j} - T_{air,j}) - \ln(T_{ow,j} - T_{air,j+1})} \tag{12}$$

**The definition of $\alpha_j$ contains the logarithmic temperature difference $\Delta_{ln} T_{air,i}$, which depends on the outer temperature of the combustion chamber. Hence, if $\alpha_j$ is known, the wall temperature can be calculated by Eq.** (11)**. To determine $\alpha_j$, a Nusselt number correlation for the annular duct flow is used:**

$$Nu_{air,j} = \frac{\alpha_{air,j}}{\lambda_{air,j}} d_{duct,h}, \tag{13}$$

with $\lambda_{air,j}$ being the thermal conductivity and $d_{duct,h}$ the hydraulic diameter of the duct (see Tab. 2). The Nusselt number does not only depend on the thermal properties but also on the flow.

There are Nusselt number correlations for turbulent and laminar flows in an annulus [49–51]. The Reynolds number of the flow in the duct is in the order of $Re_{air} = 1500 - 2000$, which is below the critical one for duct flows. However, the Reynolds number of the inflow is much higher ($\approx 20000$). Moreover, the cooling air flows through a slotted metal sheet at the beginning of the duct, which generates turbulence. Turbulence increases heat absorption significantly. A laminar model, therefore, leads to unreasonable high wall temperatures and is not applicable. Instead, a turbu-

lent flow is assumed in the cooling duct and the slots are taken as the reference for calculating the modified Reynolds number. Thus, the bulk flow velocity at the slots is taken as the characteristic velocity and $d_{duct,s} = 35\,\mathrm{mm}$ as the characteristic length. This assumption yields Reynolds numbers in the range of $Re_m = 3500 - 5000$.

The formulation of the Nusselt number in the case of Reynolds numbers between 2300 and 10000 is a mix of the correlations for laminar and turbulent flow. The Nusselt number for the annular duct then reads

$$Nu_{b,j} = (1 - \gamma_j)\, Nu_{l,j} + \gamma_j Nu_{t,j} \tag{14}$$

with the blending function $\gamma_j = (Re_{m,j} - Re_l)/(Re_t - Re_l)$. Both Nusselt numbers, the turbulent and the laminar, are adapted from the round tube by applying correction factors, which depend on the diameter ratio $a = d_{duct,i}/d_{duct,o}$. Gnielinski [52] reported the turbulent one with $Re_t = 10000$ as follows.

$$Nu_{tube,j} = \frac{\frac{\xi_j}{8} Re_t \; Pr_{air,j}}{k_1 + 12.7\sqrt{\frac{\xi_j}{8}}\left(Pr_{air,j}^{\frac{2}{3}} - 1\right)} \left(1 + \left(\frac{d_{duct,h}}{L_{cell}}\right)^{\frac{2}{3}}\right) \tag{15}$$

$$k_1 = 1.07 + \frac{900}{Re_t} - \frac{0.63}{1 + 10 Pr_{air,j}} \tag{16}$$

$$\xi_j = \left(1.8 \log\left(Re_t k_2\right) - 1.5\right)^{-2} \tag{17}$$

$\xi_j$ is the friction coefficient, which differs between the round tube and the annulus. Gnielinski [53] proposed the usage of the correction factor

$$k_2 = \frac{\left(1 + a^2\right) \ln a + \left(1 - a^2\right)}{\left(1 - a^2\right) \ln a}. \tag{18}$$

Finally, the turbulent Nusselt number for the annulus reads

$$Nu_{t,j} = 0.75\ a^{-0.17} Nu_{tube,j}. \tag{19}$$

The laminar Nusselt number is evaluated at $Re_l = 2300$ in three steps, which account for different axial phases of the flow in the duct. Since the cooling section is relatively short, all three need to be considered.

$$Nu_{l_1,j} = 3.66 + 1.2\ a^{-0.8} \tag{20}$$

$$Nu_{l_2,j} = 1.615\left(1 + 0.14\ a^{-0.5}\right)\left(Re_l\ Pr_{air,j}\frac{d_{duct,h}}{L_{cell}}\right)^{\frac{1}{3}} \tag{21}$$

$$Nu_{l_3,j} = \left(\frac{2}{1+22\,Pr}\right)^{\frac{1}{6}}\left(Re_l\ Pr_{air,j}\frac{d_{duct,h}}{L_{cell}}\right)^{\frac{1}{2}} \tag{22}$$

The mean laminar Nusselt number sums up to

$$Nu_{l,j} = \left(Nu_{l_1,j}^3 + Nu_{l_2,j}^3 + Nu_{l_3,j}^3\right)^{\frac{1}{3}}. \tag{23}$$

The medium properties in the above equations are at the mean air temperature $\overline{T}_{air,j} = \left(T_j + T_{j+1}\right)/2$. A correction of the temperature influence for the Nusselt number of the intermediate range $Nu_{b,j}$ (Eq. (14)) applies as

$$Nu_{air,j} = \left(\frac{\overline{T}_{air,j}}{T_{ow,j}}\right)^n Nu_{b,j} \tag{24}$$

with $n = 0.45$ [47]. This correction requires the unknown wall temperature $T_{ow,j}$. Thus, the Eq. (11)-(13) and (24) are solved iteratively and yield the outer wall temperature of the combustion chamber. With the final Nusselt number of the flow, all necessary quantities in the cooling duct are known.

Now, the second step evaluates the heat conduction through the wall. The known quantities from the calculations before are the amount of heat per cell $\dot{Q}_j$, and the outer wall temperature $T_{ow,j}$. The temperature difference $\Delta T_{w,j} = T_{iw,j} - T_{ow,j}$ is calculated from the heat flux as

$$\Delta T_{w,j} = \frac{\dot{Q}_j}{2\pi L_{cell}\ \lambda_{w,j}}\ \ln\left(\frac{d_{duct,i}}{D}\right) \tag{25}$$

with $D$ being the inner and $d_{duct,i}$ the outer diameter of the combustion chamber wall. The thermal conductivity $\lambda_{w,j}$ of the steel is taken at the outer wall temperature.

At last, Eq. (26) calculates the Nusselt number inside the combustion chamber from the steam's heat transfer coefficient $\alpha_{H_2O,j}$ (Eq. (27)).

$$Nu_j = \frac{\alpha_{H_2O,j}}{\lambda_{H_2O,j}} D \tag{26}$$

$$\alpha_{H_2O,j} = \frac{1}{\pi D L_{cell}}\ \frac{\dot{Q}_j}{\Delta_{ln} T_{H_2O,j}} \tag{27}$$

In these equations, the temperature distribution in the combustion chamber is required to determine the thermal conductivity $\lambda_{H_2O,j}$ and the logarithmic average temperature $\Delta_{ln} T_{H_2O,j}$. However, the temperature distribution in the combustion chamber is not measured because the adiabatic flame temperatures of up to 2500 K are too high for any thermocouple. Moreover, the actual temperature distribution in the first part of the combustion chamber is far from homogeneous. **As it generally depends on the wall distance [54], it does not serve as a useful reference. Instead, a reference temperature can be set manually. Even though, choosing different reference temperatures yields different Nusselt numbers, the Nusselt numbers of different experiments can still be compared, as long as the same reference is taken. In the best case, the reference temperature should be easy to determine. To illustrate this issue, two approaches to set this reference are compared in the results section.**

The first approach to set the reference is to assume the adiabatic flame temperature in the entire combustion chamber, which is similar to Lefebvre and Herbert [55], who used a flame bulk temperature. In this case, the logarithmic temperature difference $\Delta_{ln}T_{H_2O,j}$ is not defined and replaced by $T_{iw,j} - T_{ad}$.

Secondly, a linear temperature distribution is assumed using the boundary conditions, which are the mixing temperature $T_{mix}$ at the inlet and the exhaust temperature $T_{ex}$ 60 mm downstream of the combustion chamber. In between, the adiabatic flame temperature is set at the flame position, which was determined previously [30]. The gas temperature inside the combustion chamber interpolates linearly between these values. The model is shown in Fig. 7, together with the interpolated temperatures $T_{H_2O,j}$ at the boundaries of the evaluation cells.

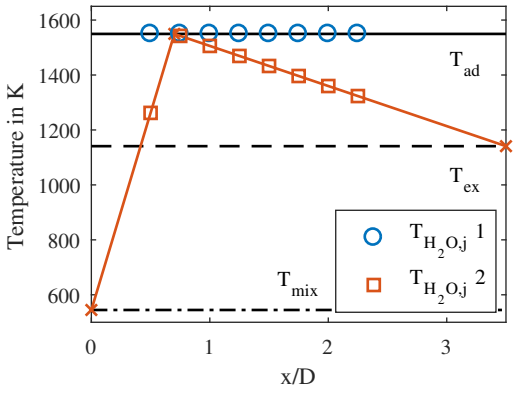


**Figure 7.** Two assumptions for the temperature in the combustion chamber: constant adiabatic flame temperature (circles) and a linear model (squares).

## 4. Results

The results are divided into two parts as well: the total heat balance of the combustion chamber system and the evaluation of the heat transfer through its wall.

### *4.1. Total Heat Balance Results*

The total heat balance of the combustion system is shown for Configuration II in Fig. 8. The flame's heat input is fixed to $P_{th} = 30\,\mathrm{kW}$. The enthalpy of the flow in the combustion chamber is increased by $\Delta\dot{H}_{cc}$, according to Eq. (4). Figure 8 (left) shows

this enthalpy gain as the lower field (yellow). The difference between the enthalpy gain and the energy provided by the flame, corresponds to the total heat loss of the system $\dot{Q}_{cc}$. **It is shown as the red field in the left plot of Fig. 8 and as the total area in the right plot.** If the system boundaries would be adiabatic, the heat flux to the cooling air should be equal to the heat loss of the combustion chamber, i.e., $\dot{Q}_{duct} \approx -\dot{Q}_{cc}$. In the actual system however, further heat losses exist via heat conduction of the metal parts (plenum, flanges, exhaust tube). Hence, the air in the cooling duct absorbs only a part of combustion chamber's heat loss. Figure 8 (right) shows $\dot{Q}_{duct}$ as the bottom field (blue). The residual heat loss $\dot{Q}_{res}$ is shown by the upper field (green) in Fig. 8 (right).

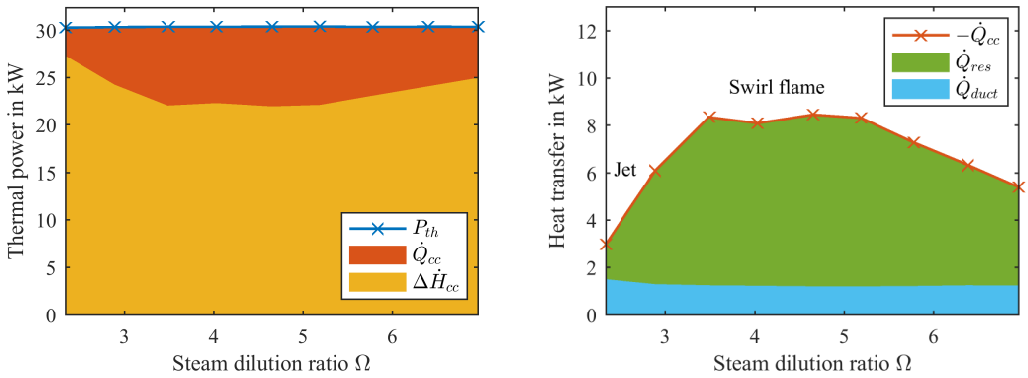


**Figure 8.** Heat balance of Configuration II at 30 kW. Left: thermal power of the flame and the enthalpy gain of the steam flow. Right: the heat loss of the combustion chamber and the heat input to the cooling air. The green field shows the residual heat loss.

The heat flux to the cooling air $\dot{Q}_{duct}$ is fairly constant as a function of the steam dilution ratio, i.e., independent of the flow patterns in the combustion chamber. **On the other hand, the residual heat loss $\dot{Q}_{res}$ is not constant but sharply increases in the jet flame mode. For low dilution ratios, the total heat loss and, in particular, the residual heat loss are very low.** This is shown in Fig 8 (right), in which the portion **of $\dot{Q}_{res}$ to** $\dot{Q}_{duct}$ is much smaller at the jet flame compared to the swirl flame. In the swirl-stabilized mode, the total heat loss is constant for increasing Ω. However, further enhancing the steam dilution lowers the temperature and raises the mass flow, **which means that more heat is convected downstream with the main flow and less transferred to the metal parts. Fig 8 (right) shows that this reduction affects only the residual heat loss,**

**not the heat flux to the cooling air.**

As stated in the methods section, the exhaust temperature is corrected to avoid radiation errors. This correction directly influences the heat loss of the combustion chamber and, thus, the residual heat loss. Figure 9 shows that the correction from $T_{ex}$ to $T_{ex,corr}$ affects mostly the high-temperature range at low steam dilution ratios. Due to the correction, the exhaust temperature gets closer to $T_{ex,ad}$, which is the ideal exhaust temperature if there would be no residual heat loss. The connection between these temperatures and the corresponding heat transfer is indicated in Fig. 9 by the face fillings, which have the same color as in Fig. 8 (right). It shows that the residual heat loss (green) declines, where the correction increases the exhaust temperature. Without the temperature correction, the residual heat loss would not demonstrate such a strong decline for low steam dilution. The low residual heat loss in this range could indicate that the temperature correction might be too intense for high temperatures. Nevertheless, a correction is necessary due to the significant heat radiation of the thermocouple material in the high-temperature range.

**Another reason for the high exhaust temperature at low $\Omega$ is that the flame is very confined in the jet mode, leading to a very hot exhaust jet in the center of the combustion chamber. This hot stream hits the thermocouple in the exhaust tube and might cause a small overestimation of the exhaust temperature due to non-uniformity. At moderate steam dilution ratios, the flame transitions to a swirl-stabilized flame and the central recirculation zone establishes in the combustion chamber. Thus, the temperature profile in the exhaust is more uniform.**

The case, shown in Fig. 8 and 9, corresponds to a constant thermal power of 30 kW. Varying the flame power leads to the three graphs in Fig. 10. The thermal power of the flame only marginally enhances the heat loss of the combustor. At 25 and 30 kW, it first increases with $\Omega$ and later slightly declines. At 20 kW the heat loss is on a similar level but nearly constant over $\Omega$. According to the right plot of Fig. 10, the heat flux to the cooling air $\dot{Q}_{duct}$ does not depend of the steam dilution ratio but increases with the thermal power. However, this effect is smaller than one would expect by increasing the thermal power by 25 and 50 %, respectively. The constant cooling flow rate seems

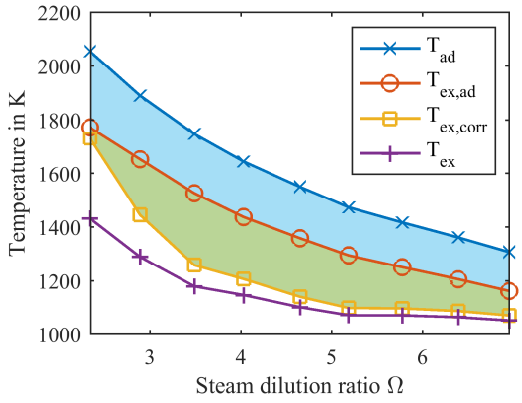


**Figure 9.** Exhaust temperature with and without correction, as well as the adiabatic flame temperature and the ideal exhaust temperature if there would be no residual heat loss.

to be the largest heat transfer resistance in the system and thus limits the absolute heat transfer from the flame to the wall.

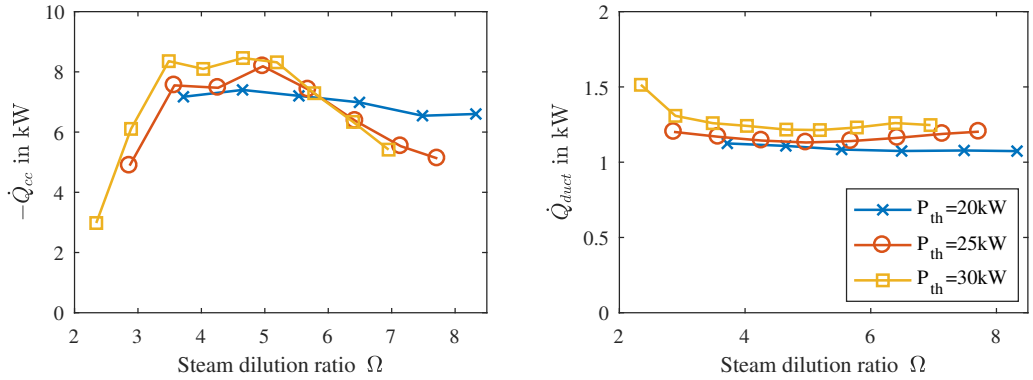


**Figure 10.** Transferred heat of Configuration II for three levels of thermal power. Left: heat loss of the combustor system $\dot{Q}_{cc}$. Right: heat absorption by the cooling air $\dot{Q}_{duct}$.

Figure 11 shows the influence of swirl intensity through the various burner configurations. All configurations show a similar trend as described before for Configuration II, but the increased swirl intensity shifts the maximum of the total heat loss $\dot{Q}_{cc}$ towards lower steam dilution ratios. In the case of Configuration IV, the maximum is already at the lowest measured Ω. Here, the flame also does not reach the jet mode because of the high swirl intensity of the steam flow.

The swirl intensity only marginally influences the $\dot{Q}_{duct}$. The heat transferred to the cooling air is slightly higher for Configuration IV probably due to an increased flame angle and a shorter distance between the flame and the wall.

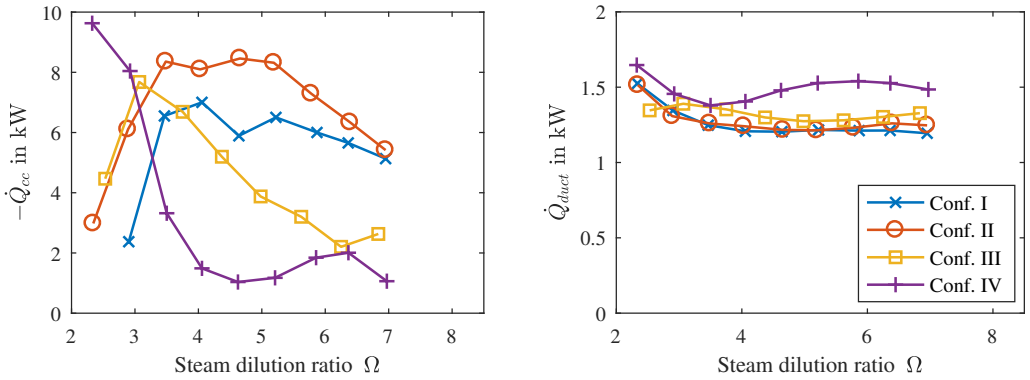


**Figure 11.** Transferred heat of different configurations for 30 kW (Configuration III: 28 kW). Left: heat loss of the combustor system $\dot{Q}_{cc}$. Right: heat absorption by the cooling air $\dot{Q}_{duct}$.

**In conclusion, the heat flux to the cooling air $\dot{Q}_{duct}$ is nearly independent from the steam dilution ratio, the thermal power and the burner configuration. It indicates that the heat flux is already limited by the heat capacity of the cooling air. Hence, water or steam should be used as coolant, if the power density of the combustor is further increased.**

### *4.2. Heat Transfer through the Wall*

**Since the determination of the wall temperatures and Nusselt numbers via the cell method is complex, it is first illustrated for one example flame (Conf. II, 30 kW, $\Omega = 4.7$) along with intermediate values of the network model. Afterwards, the influence of the steam dilution, the thermal power, and the burner configuration on the wall temperatures and the Nusselt numbers is analyzed.**

The cell method divides **the axial coordinate of the combustion chamber into small cells, as shown in Fig. 6.** Each cell corresponds to a bar in Fig. 12 (left). The height of these bars equals the enthalpy difference (Eq. (9)) **of each cell in the cooling duct**. The cells are axially bounded by the positions of the temperature sensors, which are marked by the crosses (x) in the plot. The temperature increases linearly along the length of the cooling duct. Hence, the enthalpy gain is equally distributed over the cells. Only the first cell shows a significantly higher enthalpy gain, because it is located at the flame position, i.e., the point of highest heat release.

The enthalpy gain and the cooling mass flow yield the amount of heat transferred from each combustion chamber cell to the corresponding cooling duct cell. **This heat flux** is shown as bars in Fig. 12 (right), together with the Nusselt number of each cell, acquired from the correlation in Eq. (15)-(24). The Nusselt number is nearly constant and in the order of $80-100$. Gnielinski [52] compared the correlation used in this work with experimental data for the heat transfer of air in annular ducts [51,56]. Nasiri et al. [57] and Garimella et al. [58] measured Nusselt numbers in coaxial annular ducts in the order of $60-70$ at Reynolds numbers around 10000.

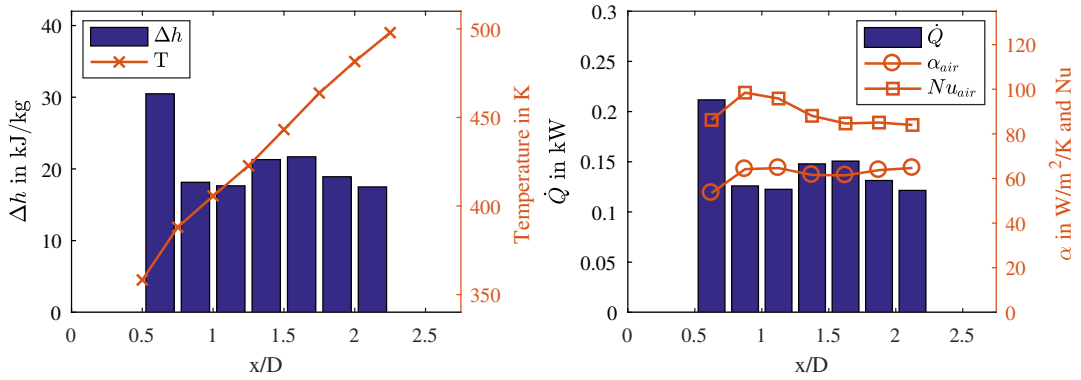


**Figure 12.** Temperature in the cooling duct (left) and Nusselt number in the evaluation cells (right) with the amount of absorbed heat in each cell. Configuration II at 30 kW and $\Omega = 4.7$. The bars refer to the left y-axis, the solid lines to the right one.

Knowing the Nusselt number and the amount of heat transferred, it is possible to calculate the outer wall temperature of the combustion chamber (Eq. 11-13). Further, the heat conduction through the wall yields the temperature difference between the inner and outer wall (Eq. 25). Figure 13 (left) shows that the temperature difference is constant and very low due to the small wall thickness. Hence, the inner and outer wall temperature can be considered the same and lie in the range of $700-900$ K. Only the first cell shows an extremely high wall temperature of 1100 K due to its increased heat flux. The position of this cell aligns well with the flame position, as the OH* intensity contour lines in the background of Fig. 13 indicate. Hence, the highest wall temperatures are reached at the point of highest heat release.

As already mentioned, the Nusselt number estimation requires a hot gas reference temperature. Figure 13 (right) shows two approaches for this reference: the constant adiabatic flame temperature and a linear model, as described in the methods section.

Both approaches show qualitatively similar results. Thereby, the linear model yields higher Nusselt numbers, especially at the flame position and in the downstream part of the combustion chamber. Choosing the adiabatic flame temperature as reference results in a nearly constant Nusselt number, except for the first cell. As both approaches deliver **qualitatively similar axial distributions**, only the constant temperature ($T_{ad}$) approach is used in the following figures. $T_{ad}$ is a well-suited reference because it can be simply calculated from the flame's operating conditions.

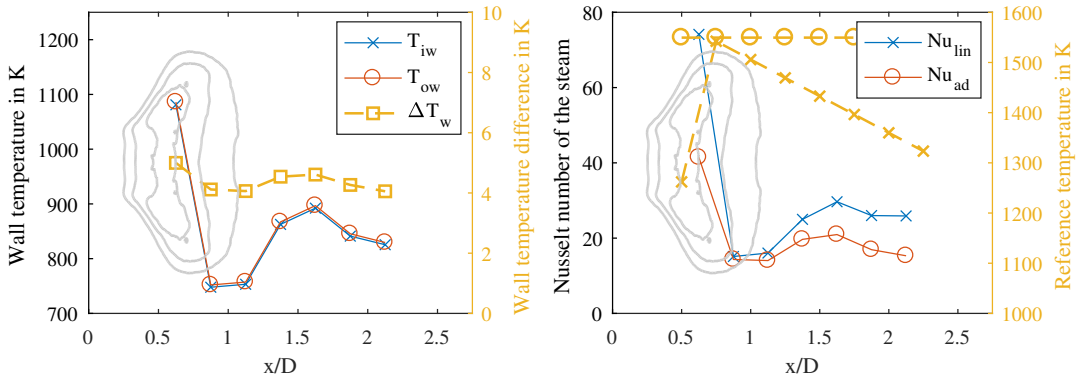


**Figure 13.** Wall temperatures (right) and Nusselt number of the steam in the combustion chamber (left) for two reference temperatures: a linear distribution (x) and the constant $T_{ad}$ (o). Configuration II at 30 kW and $\Omega = 4.7$. The solid lines refer to the left y-axis, the dashed to the right one. In the background, contours of the OH* intensity indicate the flame shape at a similar steam dilution ratio [30].

**The wall temperatures and the Nusselt numbers reveal an interesting axial distribution. The maximum is located** close to the flame position, which was also reported by Bělohradský et al. [38]. Downstream of the flame however, the wall temperature declines first, before reaching a local maximum at $x/D = 1.5$. The occurrence of the local minimum around $x/D = 1$ might be explained by the strong acceleration of the flow due to the recirculation zone and the thermal expansion. The following local maximum is located at the rear stagnation point of the recirculation zone, where the flow decelerates again.

The observations before refer to a fixed steam dilution ratio of $\Omega = 4.7$. Figure 14 shows the influence of the steam dilution on the wall temperature (left) and the Nusselt number (right). The wall temperature decreases with $\Omega$ **due to the reduced flame temperature. Contrary, the Nusselt number increases, which is caused by the increased flow rate in the combustion chamber.**

**The axial distribution of the wall temperature and the Nusselt number is qualitatively similar** at each measured thermal power and the Configurations I, II, and IV. However, the local maximum does not appear at Configuration III for an unknown reason. Surprisingly, the local maximum's position seems to be independent of the steam dilution ratio, as shown in Fig. 14. The previous studies [30,31] showed that increased steam dilution shifts the flame upstream and in radial direction. It transitions from a jet to a swirl-stabilized flame with a larger spread angle. One could assume that the point of maximum wall temperature moves upstream accordingly. However, the variation of the flame position is only about 0.2 D, which is not resolvable with the current setup since the cells have a width of 0.25 D. Additionally, the total mass flow increases with steam dilution and compensates on the flame position shift due to enhanced convection.

As the axial distribution is almost identical for each steam dilution and thermal power level, the distribution over $x/D$ is reduced to a single number by using the mean of the wall temperature and the mean Nusselt number. These quantities are shown in Figure 15 and 16 over the steam dilution ratio for different thermal power levels and different burner configurations.

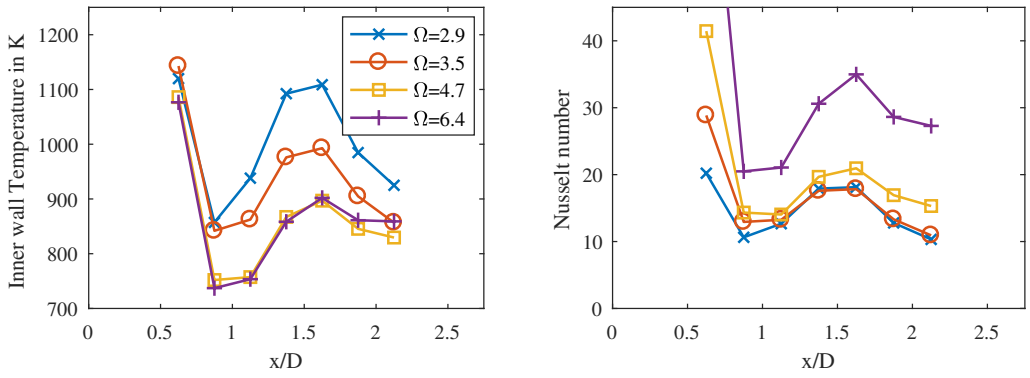


**Figure 14.** Wall temperatures (left) and Nusselt number of the steam in the combustion chamber (right) for different steam dilution ratios Ω. Configuration II at 30 kW with $T_{ad}$ as reference temperature.

**As mentioned before, the wall temperature decreases quickly with the steam dilution due the reduced flame temperature. However, the reduction saturates at $\Omega = 5$. For higher steam dilution ratios, the wall temperature stays constant. As expected, the wall temperature increases with rising**

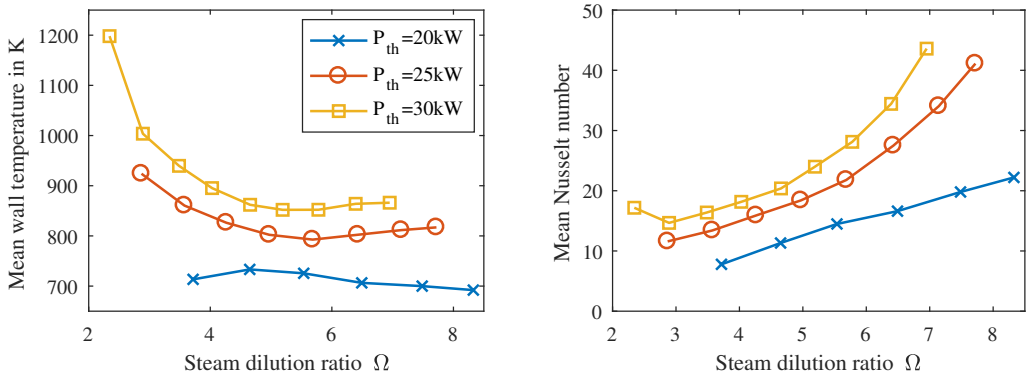


**Figure 15.** Mean wall temperatures (left) and Nusselt number of the steam in the combustion chamber (right) over the steam dilution ratio Ω. Configuration II at different power levels with $T_{ad}$ as reference temperature.

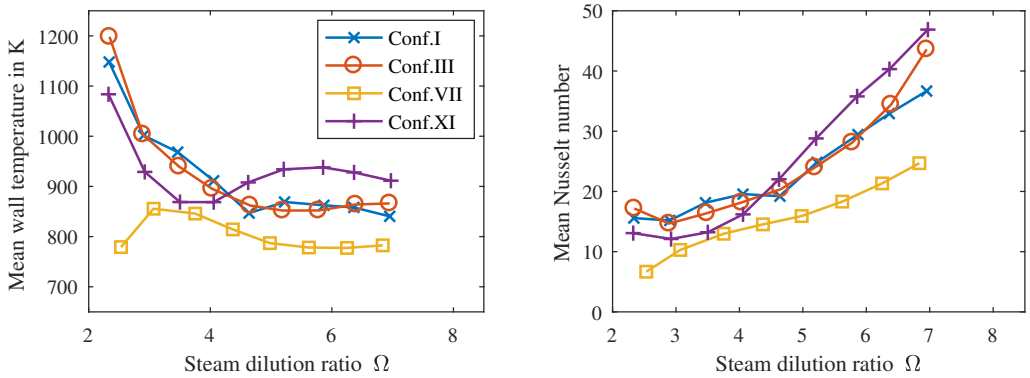


**Figure 16.** Mean wall temperatures (left) and Nusselt number of the steam in the combustion chamber (right) over the steam dilution ratio Ω. Various configurations at 30 kW with $T_{ad}$ as reference temperature.

**thermal power and reaches up to 1200 K at 30 kW. In contrast to the decline at 25 and 30 kW, the wall temperature is constant at 20 kW in the entire observed range.**

The Nusselt numbers rise with the thermal power level and even more with the steam dilution ratio. These effects probably result from the increased flow rates and turbulence in the swirl-stabilized mode.

The burner configuration, on the other hand, has no explicit influence on the wall temperatures and Nusselt numbers. The highest Nusselt numbers are reached with Configuration IV at increased steam dilution. At the same time, Configuration III shows the lowest Nusselt numbers in this range. Hence, the effect cannot be attributed to increased swirl intensity. However, all configurations provide similar trends over the steam dilution ratio for the wall temperature as well as for the Nusselt number.

Consequently, general statements can be drawn even though the absolute Nusselt numbers vary between the measurement series. At low steam dilution ratios, the combustion chamber wall has to withstand very high temperatures. Enhanced steam dilution reduces these temperatures to a certain degree, but from $\Omega = 5$ on, there is no further cooling effect to be seen in the data. The Nusselt numbers, on the other hand, grow steadily with the steam dilution.

## 5. Conclusions

This study presents, for the first time, measurements of the heat transfer in a novel swirl-stabilized hydrogen - oxygen combustor. The measurements have been conducted with the help of a steel combustion chamber, which is actively cooled by a co-flow of air in an annular duct. The first part of the study compares the total enthalpy fluxes of the combustion chamber flow and the cooling flow. It shows that only a part of the heat loss is taken up by the cooling. The residual heat is lost by heat conduction in the metal parts, i.e., the plenum and the flanges. The heat, transferred to the cooling air, increases slightly with the thermal power and when the burner's swirl intensity is enhanced. However, it remains constant over the entire range of steam dilution ratios, even though the dilution significantly reduces the adiabatic flame temperature. **This behavior indicates that the heat load of the combustor already exceeds the limits of the air's cooling capacity. In contrast, the total heat loss of the combustion chamber is not constant but shows a maximum for a certain steam dilution ratio.** For increasing swirl intensity, this maximum is shifted towards lower steam dilution ratios.

In the second part of the study, the cooling duct temperature distribution was measured to analyze the local wall temperatures and the related Nusselt numbers **by a network model**. It is found that the extremely high wall temperatures, caused by the 30 kW $H_2/O_2$ flame, can be reduced by steam dilution down to approximately 900 K. However, the cooling effect saturates at $\Omega = 5$. The Nusselt numbers are in the order of $10 - 50$ and increase with the thermal power and the steam dilution ratio.

This study is intended to assist in further developing the burner to scale it up

in power and pressure. Already at the lab-scale, the measurements show that the cooling air captures only a small portion of the combustion chamber heat loss. In more powerful systems, water or steam should be used for cooling because of the higher heat capacity. For instance, the dilution steam could be preheated by the combustor wall before entering the plenum.

## References


[1] United Nations Framework Convention on Climate Change. Paris Agreement: UN Climate Conference ; 2015.

[2] NTSO-E. Scenario outlook and adequacy forecast; 2015.

[3] MacDonald M. Impact Assessment on European Electricity Balancing Market; 2013.

[4] Bancalari E, Chan P, Diakunchak IS. Advanced hydrogen gas turbine development program. In: 23rd International Pittsburgh Coal Conference; Pittsburgh; 2006.

[5] Lam KK, Parsania N. Hydrogen enriched combustion testing of siemens SGT-400 at high pressure conditions. In: Volume 4B: Combustion, Fuels and Emissions; jun. American Society of Mechanical Engineers; 2016.

[6] Lacy B, Ziminsky W, Lipinski J, et al. Low emissions combustion system development for the GE energy high hydrogen turbine program. In: Volume 3: Combustion, Fuels and Emissions, Parts A and B; jan. ASMEDC; 2008.

[7] Asai T, Dodo S, Karishuku M, et al. Performance of multiple-injection dry low-NOx combustors on hydrogen-rich syngas fuel in an IGCC pilot plant. Journal of Engineering for Gas Turbines and Power. 2015 sep;137(9).

[8] Alavandi SK, Etemad S, Baird BD. Low single digit NOx emissions catalytic combustor for advanced hydrogen turbines for clean coal power systems. In: Volume 2: Combustion, Fuels and Emissions, Parts A and B; jun. American Society of Mechanical Engineers; 2012.

[9] Tekin N, Ashikaga M, Horikawa A, et al. Enhancement of fuel flexibility of industrial gas turbines by development of innovative hydrogen combustion systems. Gas for energy. 2018;(2):18–23.

[10] Stathopoulos P, Sleem T, Paschereit CO. Steam generation with stoichiometric combustion of H 2 / O 2 as a way to simultaneously provide primary control reserve and energy storage. Applied Energy. 2017;205(April):692–702.

[11] Cicconardi S. Steam power-plants fed by high pressure electrolytic hydrogen. International Journal of Hydrogen Energy. 2004 apr;29(5):547–551.

[12] Dybe S, Tanneberger T, Stathopoulos P. Second law analysis of an energy storage system consisting of an electrolysis plant and the graz cycle with internal h2/o2 combustion. Journal of Engineering for Gas Turbines and Power. 2019 sep;141(11).

[13] Beer S, Haidn O, Willms H. Control of stoichiometric propellant supply in an h2/o2-spinning reserve system. In: da Graça Carvalho M, editor. Combustion technologies for a clean environment : selected papers from the proceedings of the first international conference, Vilamoura, Portugal, September 3 - 6, 1991. - (Energy, combustion and the environment ;1); 1991. p. 825–838.

[14] Sternfeld HJ, Heinrich P. A demonstration plant for the hydrogen/oxygen spinning reserve. International Journal of Hydrogen Energy. 1989;14(10):703–716.

[15] Sternfeld HJ. Capacity control of power stations by O2/H2 rocket combustor technology. Acta Astronomica. 1995;37.

[16] Fröhlke K, Haidn O. Spinning reserve system based on h2/o2 combustion. Energy Conversion and Management. 1997 jul;38(10-13):983–993.

[17] Haidn OJ, Fröhlke K, Carl J, et al. Improved combustion efficiency of a h2/o2 steam generator for spinning reserve application. International Journal of Hydrogen Energy. 1998 jun;23(6):491–497.

[18] Malyshenko SP, Gryaznov A, Filatov N. High-pressure h2/o2-steam generators and their possible applications. International Journal of Hydrogen Energy. 2004 may;29(6):589–596.

[19] Malyshenko SP, Prigozhin VI, Savich AR, et al. Effectiveness of steam generation in oxyhydrogen steam generators of the megawatt power class. High Temperature. 2012 nov;50(6):765–773.

[20] Borzenko VI, Schastlivtsev AI. Efficiency of steam generation in a hydrogen-oxygen steam generator of kilowatt-power class. High Temperature. 2018 nov;56(6):927–932.

[21] Mitsugi C, Harumi A, Kenzo F. WE-NET: Japanese hydrogen program. International Journal of Hydrogen Energy. 1998 mar;23(3):159–165.

[22] Hijikata T. Research and development of international clean energy network using hydrogen energy (WE-NET). International Journal of Hydrogen Energy. 2002 feb;27(2):115–129.

[23] Bannister RL, Newby RA, Yang WC. Final report on the development of a hydrogen-fueled combustion turbine cycle for power generation. In: ASME 1998 International Gas

Turbine and Aeroengine Congress and Exhibition. American Society of Mechanical Engineers; 1998.

[24] Reichel TG, Terhaar S, Paschereit O. Increasing Flashback Resistance in Lean Premixed Swirl-Stabilized Hydrogen Combustion by Axial Air Injection. Journal of Engineering for Gas Turbines and Power. 2015;137(7).

[25] Reichel TG, Göckeler K, Paschereit O. Investigation of Lean Premixed Swirl-Stabilized Hydrogen Burner With Axial Air Injection Using OH-PLIF Imaging. Journal of Engineering for Gas Turbines and Power. 2015;137(11).

[26] Tanneberger T, Reichel TG, Krüger O, et al. Numerical Investigation of the Flow Field and Mixing in a Swirl-Stabilized Burner With a Non-Swirling Axial Jet. In: Proceedings of ASME Turbo Expo 2015; jun. ASME; 2015.

[27] Stathopoulos P, Kuhn P, Wendler J, et al. Emissions of a Wet Premixed Flame of Natural Gas and a Mixture With Hydrogen at High Pressure. Journal of Engineering for Gas Turbines and Power. 2016 nov;139(4):041507.

[28] Schimek S, Stathopoulos P, Tanneberger T, et al. Blue Combustion: Stoichiometric Hydrogen - Oxygen Combustion under Humidified Conditions. In: Proceedings of ASME Turbo Expo 2015: Turbine Technical Conference and Exposition; 2015.

[29] Tanneberger T, Schimek S, Kossatz M, et al. Development of a Swirl-Stabilized H2/O2 Combustion System under Humidified Conditions. In: Digital Proceedings of the 8th European Combustion Meeting (ECM 2017); 2017. p. 1618–1623.

[30] Tanneberger T, Schimek S, Paschereit CO, et al. Combustion efficiency measurements and burner characterization in a hydrogen-oxyfuel combustor. International Journal of Hydrogen Energy. 2019 nov;44(56):29752–29764.

[31] Tanneberger T, Schimek S, Paschereit CO, et al. Efficiency measurement approach for a hydrogen oxyfuel combustor. Journal of Engineering for Gas Turbines and Power. 2019 Sep;141(10).

[32] Patil S, Abraham S, Tafti D, et al. Experimental and numerical investigation of convective heat transfer in a gas turbine can combustor. 2009 jan;.

[33] Hedlund CR, Ligrani PM. Local swirl chamber heat transfer and flow structure at different reynolds numbers. Journal of Turbomachinery. 1999 feb;122(2):375–385.

[34] Back L, Massier P, Gier H. Convective heat transfer in a convergent-divergent nozzle. International Journal of Heat and Mass Transfer. 1964 may;7(5):549–568.

[35] Back L, Massier P, Cuffel R. Flow phenomena and convective heat transfer in a conical

supersonic nozzle. Journal of Spacecraft and Rockets. 1967;4(8):1040–1047.

[36] Witte AB, Harper EY. Experimental investigation of heat transfer rates in rocket thrust chambers. AIAA Journal. 1963;1(2):443–451.

[37] Bartz D. Turbulent boundary-layer heat transfer from rapidly accelerating flow of rocket combustion gases and of heated air. In: Advances in heat transfer. Elsevier; 1965. p. 1–108.

[38] Bělohradský P, Skryja P, Hudák I. Experimental study on the influence of oxygen content in the combustion air on the combustion characteristics. Energy. 2014 oct;75:116–126.

[39] Zhen H, Cheung C, Leung C, et al. Effects of hydrogen concentration on the emission and heat transfer of a premixed LPG-hydrogen flame. International Journal of Hydrogen Energy. 2012 apr;37(7):6097–6105.

[40] Wu L, Kobayashi N, Li Z, et al. Experimental study on the effects of hydrogen addition on the emission and heat transfer characteristics of laminar methane diffusion flames with oxygen-enriched air. International Journal of Hydrogen Energy. 2016 jan;41(3):2023–2036.

[41] Jones G, Protz C, Bullard B, et al. Local heat flux measurements with single element coaxial injectors. In: 42nd AIAA/ASME/SAE/ASEE Joint Propulsion Conference &amp Exhibit; jul. American Institute of Aeronautics and Astronautics; 2006.

[42] Bäckström D, Johansson R, Andersson K, et al. Gas temperature and radiative heat transfer in oxy-fuel flames. In: 37th International Technical Conference on Clean Coal & Fuel Systems. The Clearwater Clean Coal Conference; 2012.

[43] Andersson K, Johansson R, Johnsson F, et al. Radiation intensity of propane-fired oxy-fuel flames: Implications for soot formation. Energy & Fuels. 2008 may;22(3):1535–1541.

[44] Baukal CE, Gebhart B. Oxygen-enhanced/natural gas flame radiation. International Journal of Heat and Mass Transfer. 1997 jul;40(11):2539–2547.

[45] Cremers M, Remie M, Schreel K, et al. Heat transfer mechanisms of laminar flames of hydrogen oxygen. Combustion and Flame. 2004 oct;139(1-2):39–51.

[46] Droppers L, Schuff R, Anderson W. Study of heat transfer in a gaseous hydrogen liquid oxygen multi-element combustor. In: 43rd AIAA/ASME/SAE/ASEE Joint Propulsion Conference &amp Exhibit; jul. American Institute of Aeronautics and Astronautics; 2007.

[47] Verein Deutscher Ingenieure, VDI-Gesellschaft Verfahrenstechnik und Chemieingenieurwesen, editors. Vdi-wärmeatlas. 10th ed. Berlin u.a.: Springer; 2006.

[48] Prikopsky K. Characterization of continuous diffusion flames in supercritical water [dissertation]. ETH Zurich; 2007.

[49] Martin H. Vorlesung wärmeübertragung ii, univ. Karlsruhe (TH). 1990;.

[50] Stephan K. Wärmeübergang bei turbulenter und bei laminarer strömung in ringspalten. Chemie Ingenieur Technik. 1962 mar;34(3):207–212.

[51] Petukhov B, Roizen L. An experimental investigation of heat transfer in a turbulent flow of gas in tubes of annular section(heat transfer calculated for turbulent flow of gas in tubes of annular section). High Temperature. 1963;1:373–380.

[52] Gnielinski V. Heat transfer coefficients for turbulent flow in concentric annular ducts. Heat Transfer Engineering. 2009 may;30(6):431–436.

[53] Gnielinski V. Berechnung des druckverlustes in glatten konzentrischen ringspalten bei ausgebildeter laminarer und turbulenter isothermer strömung. Chemie Ingenieur Technik. 2007 feb;79(1-2):91–95.

[54] Bouras F, Attia MEH, Khaldi F, et al. Control of methane flame properties by hydrogen fuel addition: Application to power plant combustion chamber. International Journal of Hydrogen Energy. 2017 mar;42(13):8932–8939.

[55] Lefebvre AH, Herbert MV. Heat-transfer processes in gas-turbine combustion chambers. Proceedings of the Institution of Mechanical Engineers. 1960 jun;174(1):463–478.

[56] Kays W, Leung E, Reynolds W. Heat transfer with turbulent flow in concentric and eccentric annuli with constant and variable heat flux. 1962. 1962;.

[57] Nasiri M, Etemad S, Bagheri R. Experimental heat transfer of nanofluid through an annular duct. International Communications in Heat and Mass Transfer. 2011 aug;38(7):958–963.

[58] Garimella S, Richards DE, Christensen RN. Experimental investigation of heat transfer in coiled annular ducts. Journal of Heat Transfer. 1988 may;110(2):329–336.